

Verification of a non-hydrostatic dynamical core using horizontal spectral element method and vertical finite difference method: 2D Aspects

S. -J. Choi¹, F. X. Giraldo², J. Kim¹, and S. Shin¹,

[1]{Korea Institute of Atmospheric Prediction Systems, Seoul, Korea }

[2]{Naval Postgraduate School, Monterey, USA}

Correspondence to: S. -J. Choi (sj.choi@kiaps.org)

Abstract

The non-hydrostatic (NH) compressible Euler equations for dry atmosphere were solved in a simplified two-dimensional (2D) slice framework employing a spectral element method (SEM) for the horizontal discretization and a finite difference method (FDM) for the vertical discretization. By using horizontal SEM, which decomposes the physical domain into smaller pieces with a small communication stencil, a high level of scalability can be achieved. By using vertical FDM, an easy method for coupling the dynamics and existing physics packages can be provided. The SEM uses high-order nodal basis functions associated with Lagrange polynomials based on Gauss-Lobatto-Legendre (GLL) quadrature points. The FDM employs a third-order upwind-biased scheme for the vertical flux terms and a centered finite difference scheme for the vertical derivative and integral terms. For temporal integration, a time-split third-order Runge-Kutta (RK3) integration technique was applied. The Euler equations that were used here are in flux form based on the hydrostatic pressure vertical coordinate. The equations are the same as those used in the weather research and forecasting (WRF) model, but a hybrid sigma-pressure vertical coordinate was implemented in this model.

We validated the model by conducting the widely used standard tests: linear hydrostatic mountain wave, tracer advection, and gravity wave over Schär Mountain, density current, inertia-gravity wave, and rising thermal bubble. The results from these tests demonstrated that the horizontally spectral element vertically finite difference model is accurate and robust provided sufficient diffusion applied. The results with various horizontal resolutions also

showed convergence of second-order accuracy due to the accuracy of the time integration scheme and that of the vertical direction, although high-order basis functions were used in the horizontal. By using the 2D slice model, we effectively showed that the combined spatial discretization method of the spectral element and finite difference methods in the horizontal and vertical directions, respectively, offers a viable method for development of a NH dynamical core.

1 Introduction

There is growing interest in developing highly scalable dynamical cores using numerical algorithms under petascale computers with many cores (with the goal of exascale computing just around the corner), and the spectral element method (SEM), with high efficiency and accuracy, is known to be one of the most promising methods (Taylor et al. 1997; Giraldo 2001; Thomas and Loft 2002). SEM is local in nature because it has a large on-processor operation count (Kelly and Giraldo, 2012). SEM achieves this high level of scalability by decomposing the physical domain into smaller pieces with a small communication stencil. Additionally, SEM has been shown to be very attractive for achieving high-order accuracy and geometrical flexibility on the sphere (Taylor et al. 1997; Giraldo 2001; Giraldo et al. 2004).

To date, SEM has been implemented successfully in atmospheric modeling, such as in the community atmosphere model-spectral element (CAM-SE) dynamical core (Thomas and Loft 2005) and the scalable spectral element Eulerian atmospheric model (SEE-AM) (Giraldo and Rosmond 2004). These models consider the primitive hydrostatic equations on global-grids, such as a cubed-sphere tiled with quadrilateral elements using SEM in the horizontal discretization and the finite difference method (FDM) in the vertical. The robustness of SEM has been illustrated through three-dimensional dry dynamical test cases (Giraldo and Rosmond 2004; Giraldo 2005; Thomas and Loft 2005; Taylor et al. 2007; Lauritzen et al. 2010).

The ultimate objective of our study is to build a 3D non-hydrostatic (NH) model based on the compressible Navier-Stokes equations using combined horizontally SEM and vertically FDM. Because testing a 3D NH model requires a large amount of computing resources, studying the feasibility of our approach in 2D is an attractive alternative to the development of a fully 3D model. This is the case because a 2D slice model can effectively test the

1 practical issues resulting from the vertical discretization and time integration prior to
2 construction of a full 3D model. Although we could discretize the vertical direction using
3 SEM (as proposed in Kelly and Giraldo 2012 and Giraldo et al. 2013), we chose to use a finite
4 difference method for discretization in the vertical direction because it provides an easy way
5 to couple the dynamics and existing physics packages.

6 For this objective, we developed a dry 2D NH compressible Euler model based on SEM
7 along the x direction and FDM along the z direction, which we hereafter refer to as the 2D
8 NH model. We adopted the governing equation formulation proposed by Skamarock and
9 Klemp (2008) (hereafter, SK08), which is used in the weather research and forecasting (WRF)
10 model. The Euler equations are in flux form based on the hydrostatic pressure vertical
11 coordinate. In SK08, the terrain-following sigma-pressure coordinate is used, but we here
12 employed a hybrid sigma-pressure vertical coordinate. Park et al. (2013) (hereafter, PK13)
13 provided a clue for the equation set in the hybrid sigma-pressure in their appendix, in which
14 the hybrid sigma-pressure coordinate is applied to the hydrostatic primitive equations and can
15 be modified exactly to the sigma-pressure coordinate at the level of the actual coding
16 implementation. We also built the 2D NH model using a time-split third-order Runge-Kutta
17 (RK3) for the time discretization, which has been shown to be effective in the WRF model.
18 We kept the temporal discretization of the model as similar as possible to the WRF model in
19 order to more directly discern the differences related to the discrete spatial operators between
20 the two models. This provides robust tools for development and verification of the 2D NH
21 model.

22 In this paper, we demonstrate the feasibility of the 2D NH model by conducting
23 conventional benchmark test cases and by focusing on the description of the numerical
24 scheme for the spatial discretization. We verify the 2D NH by analyzing four test cases:
25 inertia-gravity wave, rising thermal bubble, density current wave, and linear hydrostatic
26 mountain wave.

27 The organization of this paper is as follows. In the next section, we describe the
28 governing equations with definitions of the prognostic and diagnostic variables used in our
29 model. In section 3, we explain the temporal and spatial discretization including the spectral
30 element formulation. In section 4, we present the results of the 2D NH model using all four
31 test cases, and finally, in section 5, we summarize the paper and propose future directions.

2 Governing Equations

We adopted the formulation of the governing-equation set of SK08. Here, we implemented the hybrid sigma-pressure coordinate introduced in PK13, which considers only the hydrostatic primitive equation. The hybrid sigma pressure coordinate is defined with $\eta \in [0, 1]$ as

$$\rho_d = B(\eta)(\rho_s - \rho_t) + [\eta - B(\eta)](\rho_0 - \rho_t) + \rho_t, \quad (1)$$

where ρ_d is the hydrostatic pressure of dry air, $B(\eta)$ is the relative weighting of the terrain-following coordinate versus the normalized pressure coordinate, ρ_s , ρ_t , and ρ_0 are the hydrostatic surface pressure of dry air, the top level pressure, and a reference sea level pressure, respectively. A more detailed description of the hybrid sigma-pressure coordinate can be found in the Appendix of PK13. The definition of the flux variables are

$$(\vec{V}_H, W, \Omega, \Theta) = \mu_d \times (\vec{v}_H, w, \dot{\eta}, \theta), \quad (2)$$

where $\vec{v}_H = (u, v)$ and w are the velocities in the horizontal and vertical directions, respectively, $\dot{\eta} \equiv \frac{d\eta}{dt}$ is the η -coordinate (contravariant) vertical velocity, θ is the potential temperature, and μ_d is the mass of the dry air in the layers defined as

$$\mu_d(x, y, \eta, t) = \frac{\partial \rho_d}{\partial \eta} = \frac{\partial B(\eta)}{\partial \eta}(\rho_s - \rho_t) + \left[1 - \frac{\partial B(\eta)}{\partial \eta}\right](\rho_0 - \rho_t). \quad (3)$$

The flux-form Euler equations for dry atmosphere to be recast using perturbation variables are expressed as

$$\frac{\partial \vec{V}_H}{\partial t} = -\mu_d (\nabla_\eta \phi' + \alpha_d \nabla_\eta \rho' + \alpha'_d \nabla_\eta \bar{\rho}) - \left(\frac{\partial \rho'}{\partial \eta} - \mu'_d \right) \nabla_\eta \phi - \nabla_\eta \cdot (\vec{V}_H \otimes \vec{V}_H) - \frac{\partial (\Omega \vec{V}_H)}{\partial \eta} + F_{\vec{V}_H}, \quad (4)$$

$$\frac{\partial W}{\partial t} = g \left[\frac{\partial \rho'}{\partial \eta} - \mu'_d \right] - \nabla_\eta \cdot (\vec{V}_H W) - \frac{\partial (\Omega W)}{\partial \eta} + F_W, \quad (5)$$

$$\frac{\partial \mu'_d}{\partial t} = \frac{\partial}{\partial t} \left(\frac{\partial \rho'_d}{\partial \eta} \right) = \frac{\partial B(\eta)}{\partial \eta} \frac{\partial \rho'_s}{\partial t} = -\nabla_\eta \cdot \vec{V}_H - \frac{\partial \Omega}{\partial \eta}, \quad (6)$$

$$\frac{\partial \phi'}{\partial t} = -\frac{1}{\mu_d} \left[\vec{V}_H \cdot \nabla_\eta \phi + \Omega \frac{\partial \phi}{\partial \eta} - gW \right], \quad (7)$$

$$\frac{\partial \Theta}{\partial t} = -\nabla_\eta \cdot (\vec{V}_H \theta) - \frac{\partial (\Omega \theta)}{\partial \eta}, \quad (8)$$

where ϕ is the geopotential, α_d is the inverse density for dry air, and $F_{\vec{V}_H}$ and F_W represent forcing terms of Coriolis and curvature, which we ignore for simplicity. In Eqs. (4)–(8), the governing equations are described with perturbation variables, such as $\rho = \bar{\rho}(\bar{z}) + \rho'$, $\phi = \bar{\phi}(\bar{z}) + \phi'$, $\alpha_d = \bar{\alpha}_d(\bar{z}) + \alpha'_d$, and $p_s = \bar{p}_s(x, y) + p'_s$, where the variables denoted by an overbar are the reference state variables that satisfy hydrostatic balance.

For completeness, the diagnostic relation for Ω is given by integrating Eq. (6) vertically from the surface ($\eta = 1$) to the material surface:

$$\Omega = -\int_1^\eta \left(\frac{\partial B(\eta)}{\partial \eta} \frac{\partial p'_s}{\partial t} + \nabla_\eta \cdot \vec{V}_H \right) d\eta, \quad (9)$$

where $\frac{\partial p'_s}{\partial t}$ is obtained by integrating Eq. (6) vertically from the surface ($\eta = 1$) to the top ($\eta = 0$) using a no-flux boundary condition, such as $\Omega|_{\eta=0 \text{ or } 1} = 0$. $\frac{\partial p'_s}{\partial t}$ is defined as

$$\frac{\partial p'_s}{\partial t} = -\int_{\eta=0}^{\eta=1} (\nabla \cdot \vec{V}_H) d\eta. \quad (10)$$

The above equation allows p'_s to be evolved forward in time where we then compute μ'_d directly from Eq. (5). The diagnostic relation for the dry inverse density is given as

$$\frac{\partial \phi'}{\partial \eta} = -\bar{\mu}_d \alpha'_d - \alpha_d \mu'_d, \quad (11)$$

and the full pressure for dry atmosphere is

$$\rho = \rho_0 \left(\frac{R_d \theta}{\rho_0 \alpha_d} \right)^{c_p/c_v}. \quad (12)$$

This concludes the description of the governing equations used in our model; in the next section, we describe the discretization of the continuous form of the governing equations that are used in our model.

3 Discretization

3.1 Spatial discretization

1) Horizontal direction

For a given η level, we discretized the horizontal operators using SEM. Therefore, in the 2D (x-z) slice framework, we focus on the SEM discrete gradient operator for 1D (x). In SEM, we approximate the solution in non-overlapping elements Ω^e as

$$q(x, t) = \sum_{i=1}^{N+1} \psi_i(x) q_N(x_i, t), \quad (13)$$

where x_i represents the $N+1$ grid points that correspond to the Gauss-Lobatto-Legendre (GLL) points and $\psi_i(x)$ are the N th-order Lagrange polynomials based on the GLL points. It is noteworthy that the ψ_i have the cardinal property, i.e., they can be represented as Kronecker delta functions where ψ_i are zero at all nodal points except x_i .

The GLL points ξ_i in a reference coordinate system $\xi \in [-1, +1]$ and the associated quadrature weights $\omega(\xi_i)$,

$$\omega(\xi_i) = \frac{2}{N(N+1)} \left[\frac{1}{P_N(\xi_i)} \right]^2, \quad (14)$$

are introduced for the Gaussian quadrature:

$$\int_{\Omega^e} q \, d\Omega^e = \int_{-1}^{+1} q(\xi) |J(\xi)| \, d\xi \approx \sum_{i=0}^N \omega(\xi_i) q(\xi_i) |J(\xi_i)|, \quad (15)$$

where $P_N(\xi)$ are the N th-order Legendre polynomials, $J = \frac{\partial x}{\partial \xi}$ is the transformation Jacobian, and Ω^e represents the non-overlapping elements.

We now introduce the polynomial expansions into our governing equations in the form

$$\frac{\partial q}{\partial t} = -F(q), \quad (16)$$

multiply by the basis function ψ_i as a test function, and integrate to yield a system of ordinary differential equations, such as

$$M_{ji}^e \frac{dq_i}{dt} = - \int_{\Omega_e} \psi_j F \left(\sum_{i=1}^{N+1} \psi_i(\xi) q_i \right) d\xi, \quad (17)$$

where $i = 1, 2, \dots, N+1$, M_{ji}^e is the element-based mass matrix given as

$$M_{ji}^e = \int_{\Omega_e} \psi_j \psi_i d\xi = \omega_j |J_j| \delta_{ji}. \quad (18)$$

The right-hand sides of Eqs. (17) and (18) are evaluated using the Gaussian quadrature of Eq. (15). It is noted that using GLL points for both interpolation and integration results in a diagonal mass matrix M_{ji}^e , which means that the inversion of the mass matrix is trivial.

The horizontal derivatives included in the right-hand side of Eq. (17) are evaluated using the analytic derivatives of the basis functions as follows:

$$\frac{\partial q}{\partial x} = \frac{\partial q}{\partial \xi} \frac{\partial \xi}{\partial x} = \frac{\partial}{\partial \xi} \left[\sum_{i=1}^{N+1} \psi_i(\xi) q_i \right] \frac{\partial \xi}{\partial x} = \left[\sum_{i=1}^{N+1} \frac{\partial \psi_i}{\partial \xi} q_i \right] \frac{1}{|J|}. \quad (19)$$

Note that the non-differential operations, such as cross products, are computed directly at grid points since we use nodal basis functions associated with Lagrange polynomials based on the GLL points. In order to satisfy the equations globally, we use the direct stiffness summation (DSS) operation. For a more detailed description of the SEM, see Giraldo and Rosmond (2004), Giraldo and Restelli (2008), and Kelly and Giraldo (2012).

2) Vertical direction

Using a Lorenz staggering, the variables \vec{V}_H , Θ , μ , α , p are at layer midpoints denoted by $k = 1, 2, \dots, K$, where K is the total number of layers, and the variables W , Ω , and ϕ are at layer interfaces defined by $k + \frac{1}{2}$, $k = 0, 1, \dots, K$ so that $\eta_{K+1/2} = \eta_{top}$ and $\eta_{1/2} = \eta_{Bottom} = 1$. Fig. 1 describes the grid points and the allocation of the variables. Here, we

evaluate the vertical advection terms $\left(\frac{\partial(\Omega \vec{V}_H)}{\partial \eta}, \frac{\partial(\Omega W)}{\partial \eta}, \text{ and } \frac{\partial(\Omega \theta)}{\partial \eta} \right)$ and vertical derivative

terms $(\frac{\partial \rho'}{\partial \eta}$ and $\frac{\partial \phi}{\partial \eta})$. The former is discretized using the third-order upwind-biased discretization in Hundsdorfer et al. (1995) which is given as

$$\left. \frac{\partial f}{\partial \eta} \right|_k = \frac{f_{k-2} - 8f_{k-1} + 8f_{k+1} - f_{k+2}}{12\Delta\eta} + \text{sign}(\Omega) \frac{f_{k-2} - 4f_{k-1} + 6f_k - 4f_{k+1} + f_{k+2}}{12\Delta\eta}, \quad (20)$$

where f corresponds to the flux, such as $\Omega \vec{v}_H$, and $\Delta\eta = \eta_{k+1/2} - \eta_{k-1/2}$ is the thickness of the layer. The latter is discretized by the centered finite difference, which is given as

$$\left. \frac{\partial g}{\partial \eta} \right|_k = \frac{g_{k+1/2} - g_{k-1/2}}{\Delta\eta}, \quad (21)$$

where g corresponds to the variables ρ' and ϕ . Likewise, the vertical discretization integration rules for the calculations of Eqs. (9) and (10) follow the finite difference naturally as

$$\int q d\eta = \sum_k q_{k+1/2} (\eta_{k+1} - \eta_k). \quad (22)$$

3) Explicit diffusion

In addition to the governing equations, a viscous term could be needed to conduct some tests. The viscosity used here is an explicit Laplacian (∇^2) diffusion operator on coordinate surfaces. In order to implement the Laplacian operator $f = \nu_h \frac{\partial^2}{\partial X^2} (\mu_d a)$ for a model flux variable $\mu_d a$, we multiply by the basis function ψ as a test function and integrate using the divergence theorem to yield the weak form equation:

$$\int_{\Omega^e} \psi f \, d\Omega^e = K_h \left(\int_{\Gamma^e} \psi \frac{\partial}{\partial X} (\mu_d a) \, d\Gamma^e - \int_{\Omega^e} \frac{\partial}{\partial X} \psi \cdot \frac{\partial}{\partial X} (\mu_d a) \, d\Omega^e \right), \quad (23)$$

where ν_h denotes the eddy viscosity coefficient and the term with Γ^e is a boundary integral that accounts for internal faces (neighboring elements share faces). Because we used the periodic boundary condition in this study, the boundary integral term of the right-hand sides can be ignored in all elements, which allows us to rewrite the equations as

$$\int_{\Omega^e} \psi f \, d\Omega^e = -\nu_h \int_{\Omega^e} \frac{\partial \psi}{\partial x} \frac{\partial}{\partial x} (\mu_d a) \, d\Omega^e. \quad (24)$$

After introducing the polynomial expansions, such as $a(x, t) = \sum_{i=1}^{N+1} \psi_i(x) a_N(x_i, t)$, the integrals of the above equation can be approximated using SEM. A description of the Laplacian operator using SEM can also be found in Denis et al. (2011). The vertical Laplacian operator for a model flux variable $\mu_d a$ is added to a governing equation as follows:

$$\frac{\partial}{\partial t} (\mu_d a) = \dots + \nu_v g^2 (\mu_d \alpha)^{-1} \frac{\partial}{\partial \eta} \left((\mu_d \alpha)^{-1} \frac{\partial (\mu_d a)}{\partial \eta} \right), \quad (25)$$

where ν_v denotes the vertical eddy viscosity coefficient and α is the inverse density. It is noted that the above term is not more than $\nu_v \frac{\partial^2 (\mu_d a)}{\partial z^2}$. The vertical derivative term $\frac{\partial}{\partial \eta}$ is discretized by the centered finite difference.

3.2 Temporal discretization

To integrate the equations, we used the time-split RK3 integration technique following the strategy of SK08. In the time-split RK3 integration, low-frequency modes due to advective forcings are explicitly advanced using a large time step in the RK3 scheme, but high-frequency modes are integrated over smaller time steps. Among the high-frequency modes, horizontally propagating acoustic/gravity waves are advanced using an explicit forward-backward time integration scheme and vertically propagating acoustic waves and buoyancy oscillations are advanced using a fully implicit scheme (Klemp et al. 2007). For numeric stability, acoustic-mode filterings of the forward centering of the vertically implicit portion and divergence damping of the horizontal momentum equation are used, which is the same as in the WRF model (Skamarock et al. 2008). It is notable that the time-split RK3 integration scheme is third-order accurate for linear equations and second-order accurate for nonlinear equations (SK08).

This technique has been shown to work effectively within numerous non-hydrostatic models including the WRF model (Skamarock et al. 2008), the model for prediction across scales (MPAS) (Skamarock et al. 2012), and the non-hydrostatic icosahedral atmospheric model (NICAM) (Sato et al. 2008). It is also noted that in the procedure of the time-split RK3 integration, the difference between the approach used in this paper and that in SK08 comes from the vertical coordinate. Since we use the hybrid sigma-pressure coordinate, the equation for p'_s (Eq. (6)) should be first stepped forward in time using forward-backward differencing on the small time steps, then μ'_g can be computed directly from the specification of the vertical coordinate in Eq. (9) and Ω can be obtained from the vertical integration.

4 Test cases

We validated the 2D NH model with five test cases: linear hydrostatic mountain wave and tracer-advection and gravity-wave tests over Schär Mountain, as well as density current, inertia-gravity wave, and rising thermal bubble experiments. The last three cases do not have analytic solutions. Therefore, for the mountain experiments, the numerical results of the 2D NH model were compared with analytic solutions (Durran and Klemp 1983; Schär et al. 2002); for the other experiments, we compared our results with the results of other published papers.

It should be mentioned that the horizontal SEM formulation is able to utilize arbitrary-order polynomials per element to represent the discrete spatial operators, but in this paper all the results presented use either 5th- or 8th-order polynomials. The averaged horizontal grid spacing is defined as

$$\Delta\bar{x} = \frac{\sum_{n=1}^N \Delta x_n}{N}, \quad (26)$$

where Δx_n is the internal grid spacing within the element, which is regularly spaced in the domain, and N is the number of intervals associated with irregularly spaced GLL quadrature points, which is equivalent to the order of the basis polynomials. The average vertical grid spacing is defined as in Eq. (26). Below, we use this convention to define the grid resolution. The resolutions and time-step sizes used for all the cases are summarized in Table 1.

4.1 Linear hydrostatic mountain wave test

We simulated the linear hydrostatic mountain wave test introduced by Durran and Klemp (1983) (hereafter, DK83) in which the analytic steady-state solution is provided by using a single-peak mountain with uniform zonal wind. To compare our results with the analytic and numerical solutions shown in DK83, the 2D NH was initialized using the same initial conditions and mountain profile as in DK83, and we analyzed our results using the same metrics as DK83.

The mountain profile is given by

$$h(x) = \frac{h_m}{1 + \left(\frac{x - x_c}{a_m} \right)^2}, \quad (27)$$

where the half-length of the mountain a_m is 10 km, the height h_m is 1 m, and the prescribed center x_c of the profile is 0 km. The initial temperature is $T_0 = 250$ K for an isothermal atmosphere with the uniform zonal wind $\bar{u} = 20$ m/s. In the isothermal case, the Brunt-Väisälä frequency $N^2 = g \frac{d(\ln \bar{\theta})}{dz} \approx \frac{g^2}{c_p T_0}$ yields the potential temperature as

$$\bar{\theta} = \theta_0 e^{\frac{g}{c_p T_0} z}, \quad (28)$$

which is one of the prognostic variables in our model. The domain is defined as $(x, z) \in [-300, 300] \times [0, 30]$ km². The bottom boundary uses a no-flux boundary condition, whereas the lateral and top boundaries use sponge layers. The sponged zone is 10 km deep from the top and 50 km wide from the lateral boundaries. Over the sponge-layer zone, the prognostic variables are relaxed to the basic initial hydrostatic state. The model is integrated with a grid resolution of $\Delta \bar{x} = 2$ km using 5th-order basis polynomials per element and $\Delta \bar{z} = 375$ m for a nondimensional time of $\frac{\bar{u} t}{a} = 60$, which corresponds to 8.33 hours.

Additionally, the model is run without diffusion or viscosity.

Fig. 2 shows the numerical and analytic solutions at steady state for the horizontal and vertical velocities, which agree reasonably well. The vertical velocity fields match very closely, although the extrema in the horizontal velocity field are underestimated by the

numerical model. The underestimated extrema in the horizontal velocity were also shown in both models of DK83, which used $\Delta x = 2$ km and $\Delta z = 200$ m, and in Giraldo and Restelli (2008) (hereafter, GR08), which used $\Delta \bar{x} = 1.2$ km and $\Delta \bar{z} = 240$ m with 10th-order basis polynomials. Our result in the horizontal velocity is in good agreement with DK83 and GR08.

To check the vertical transport of horizontal momentum, Fig. 3 shows the normalized momentum flux values at various times. It is observed that the flux has developed well and that the simulations reach steady-state after $\frac{\bar{u}t}{a} = 60$. It is also noted that the mean momentum flux at this time is 97% of its analytic value. The result agrees well with DK83 as well as GR08; however, it is important to point out that the Durran-Klemp model is based on the FD method in both directions while the Giraldo-Restelli model is based on SEM in both directions. The mountain test shows that the terrain-following vertical coordinate is well suited for the combination of horizontal SEM and vertical FDM for spatial discretization, even though we considered a small mountain.

4.2 Tracer-advection, resting atmosphere and gravity-wave tests over Schär Mountain

In order to verify the feasibility of 2D NH to treat steep surface elevations associated with the vertical terrain-following coordinate, we performed the tracer-advection and gravity-wave experiments introduced by Schär et al. (2002) (hereafter, SC02), in which the mountain is defined by a five-peak mountain chain, over Schär Mountain. To compare our results with the numerical solution shown in SC02, the initial conditions and mountain profiles for the tracer-advection and gravity-wave experiments are the same as those of SC02. Additionally, we conducted a simulation for a resting, stratified atmosphere over Schär Mountain to show how spurious velocities are leaded by the model.

For the tracer-advection test, the mountain profile is given by

$$h(x) = \begin{cases} h_0 \cos^2\left(\frac{\pi x}{\lambda}\right) \cos^2\left(\frac{\pi x}{2a}\right) & \text{for } |x| \leq a \\ 0 & \text{for } |x| \geq a \end{cases}, \quad (29)$$

where $h_0 = 3$ km, $a = 25$ km, and $\lambda = 8$ km. The prescribed wind profile is given by

$$u(z) = u_0 \begin{cases} 1 & \text{for } z_2 \leq z \\ \sin^2\left(\frac{\pi}{2} \frac{z - z_1}{z_2 - z_1}\right) & \text{for } z_1 \leq z \leq z_2 \\ 0 & \text{for } z \leq z_1 \end{cases} , \quad (30)$$

where $u_0 = 10 \text{ m s}^{-1}$, $z_1 = 4 \text{ km}$, and $z_2 = 5 \text{ km}$, and the initial tracer is assigned as

$$q(x, z) = q_0 \begin{cases} \cos^2\left(\frac{\pi r}{2}\right) & \text{for } r \leq 1 \\ 0 & \text{else} \end{cases} \quad \text{with } r = \left[\left(\frac{x - x_0}{A_x} \right)^2 + \left(\frac{z - z_0}{A_z} \right)^2 \right]^{1/2} , \quad (31)$$

where amplitude $q_0 = 1$, location $(x_0, z_0) = (-50, 9) \text{ km}$, and the half-width $(A_x, A_z) = (25, 3) \text{ km}$. Since the domain is defined as $(x, z) \in [-150, 150] \times [0, 25] \text{ km}^2$, the tracer is centered directly over the mountain at time 2500 s. The model is integrated with a grid resolution of $\Delta \bar{x} = 300 \text{ m}$ using 5th-order basis polynomials per element and $\Delta \bar{z} = 250 \text{ m}$ using 100 levels for 5000 s. The model is run without any diffusion, filter, or limiter. It should be noted that the advection equation used in this study is the advective form defined as

$$\frac{\partial q}{\partial t} = -\left(u \frac{\partial q}{\partial x} + \dot{\eta} \frac{\partial q}{\partial \eta} \right) . \quad (32)$$

The numerical solutions and the error field are shown in Fig. 4. The figure uses the same contouring interval as in SC02. Even at $t = 2500 \text{ s}$, at which the center of the tracer is located over the center of the mountain, the distribution of the initial tracer is generally maintained (Fig. 4a), which means that 2D NH using the horizontal spectral element method and vertical finite difference method can produce numerical solutions of good quality in response to the strong vertical gradient in the coordinate deformation. It is noteworthy in Fig. 4b that the error at $t = 5000 \text{ s}$ gives ranges of $[-2.71 \times 10^{-2}, 2.35 \times 10^{-2}]$, which are substantially small, and that the error is distributed mainly over the mountain where distortion of the computational grid is significant.

Simulations for the resting atmosphere and the gravity-wave over Schär mountain were initialized in a stratified atmosphere with the Brunt-Väisälä frequency of $N = 0.01 / \text{s}$ and the initial temperature of $T_0 = 288 \text{ K}$. The gravity-wave test had the constant mean flow of

$\bar{u} = 10$ m/s in addition to the initial condition of the resting atmosphere test. In these simulations, the highest mountain peak was $h_0 = 250$ m, which is relatively lower than that in the advection test. The mountain profile is given by

$$h(x) = h_0 \exp \left[- \left(\frac{x}{a} \right)^2 \right] \cos^2 \left(\frac{\pi x}{\lambda} \right), \quad (33)$$

where $a = 5$ km and $\lambda = 4$ km, and the domain is defined as $(x, z) \in [-30, 30] \times [0, 21]$ km². The model was integrated with a grid resolution of $\Delta \bar{x} = 300$ m using 5th-order basis polynomials per element and $\Delta \bar{z} = 250$ m using 80 levels. The bottom boundary had a no-flux boundary condition. For the resting atmosphere test, the model is integrated in a long-time for 25 days. We employed a dynamic viscosity of $\nu = 40$ m²s⁻¹ on coordinate surfaces to remove erroneous oscillations at the small scale, which was inevitably needed for this simulation to remain stable. The numerical diffusion was applied for momentum and potential temperature along the horizontal direction. For the Schär mountain gravity-wave test, the model is integrated for 10 h without any viscosity, but the lateral and top boundaries had sponge layers. The sponged zone was 10 km deep from the top and 5 km wide from the lateral boundaries. Over the sponge layer zone, the prognostic variables were relaxed to the initial state.

Fig. 5 shows the time evolution of the maximum vertical velocities for the resting-atmosphere simulation. We observe that the maximum vertical velocity abruptly increases by 0.08 ms⁻¹ at 1.5 h. But, it is noted that after 2 h the maximum vertical velocity seems to reach a state of equilibrium by about 0.29 ms⁻¹ and tends to increase steadily until 25 days. Fig. 6 shows the simulated results of the perturbed horizontal and vertical wind speeds after 10 h for the Schär mountain gravity-wave. In comparison with the analytic solution, the numerical solutions match quite well. The results of the present model are also very similar to the results of other numerical models (Giraldo and Restelli 2008; Li et al 2013). For a quantitative comparison, we present the root-mean-square errors for u' , w' , and θ' in Table 2. These values are very comparable with those of other numerical models (Giraldo and Restelli 2008; Li et al 2013).

4.3 2D density current test

In order to verify the feasibility of 2D NH to control oscillations with numerical viscosity and evaluate numerical schemes in 2D NH, we conducted the density current test suggested by Straka et al. (1993). The density current test is initialized using a cold bubble in a neutrally stratified atmosphere. When the bubble touches the ground, the density current wave starts to spread symmetrically in the horizontal direction forming Kelvin-Helmholtz rotors. Following Straka et al. (1993), we employed a dynamic viscosity of $\nu = 75 \text{ m}^2\text{s}^{-1}$ to obtain converged numerical solutions. The viscosity used here is an explicit Laplacian (∇^2) diffusion operator on coordinate surfaces.

For an initial cold bubble, the potential temperature perturbation is given as

$$\theta' = \frac{\theta_c}{2} [1 + \cos(\pi r)], \quad (34)$$

where $\theta_c = -15 \text{ K}$ and $r = \sqrt{\left(\frac{x - x_c}{x_r}\right)^2 + \left(\frac{z - z_c}{z_r}\right)^2}$, with the center of the bubble at $(x_c, z_c) = (0, 3000) \text{ m}$ and the size parameter $(x_r, z_r) = (4000, 2000) \text{ m}$. No-flux boundary conditions were used for all boundaries, and the model was integrated for 900 s on the domain $[-25600, 25600] \times [0, 6400] \text{ m}^2$. In this study, the potential temperature perturbation of $\theta_c = -15 \text{ K}$ was adopted for comparison with GR08 and Li et al. (2013). Straka et al. (1993) originally used a -15 K temperature perturbation. The -15 K potential temperature corresponds to -13.53 K temperature.

Fig. 7 shows the potential temperature perturbation after 900 s for 400-, 200-, 100-, and 50-m grid spacings ($\Delta\bar{x}$) using 5th-order basis polynomials per element. All simulations used $\Delta\bar{z} = 64 \text{ m}$ grid spacing vertically. As expected, the higher-resolution experiments produced better solutions than the lower-resolution experiments. At the very lowest resolution of 400 m, only two of the three Kelvin-Helmholtz rotors were generated with somewhat coarsened frontal surfaces. In the experiment with a resolution of 200 m, the three rotors appeared, but the numerical solution still suffered from the coarsening of frontal surfaces. The solutions on grids finer than 100 m converged with the three rotor structures adequately simulated. The converged solution was almost identical to other published solutions (e.g., Straka et al. 1993; Skamarock and Klemp 2008; GR08).

In order to show the effect of higher order of the basis polynomials, we show the potential temperature perturbations using 8th-order basis polynomials per element with the same number of GLL grid points in the physical domain as the simulations using 5th-order basis polynomials (Fig. 8). This was achieved by using a lower number of elements in 8th-order experiment than in the 5th-order experiment as the number of grid points at a given level becomes $ne \times np$, in which ne refers to the number of elements and np denotes the polynomial order of the elements. The simulation with 8th-order basis polynomials at the very lowest resolution of 400 m reproduced the converged solution more closely than the simulation with 5th-order basis polynomials. Even in the 200-m resolution experiment, the coarsening frontal surfaces were mitigated and the solution was similar with the converged solution with three rotors.

Fig. 9 shows profiles of the potential temperature perturbation at the height of 1200 m. The results from the highest grid resolution of the simulations using 5th- and 8th-order basis polynomials are indistinguishable and well converged (Fig. 9a). Three minima corresponding to the three rotors agree well with other published solutions. In addition to the profiles, the front location (-1 K of potential temperature perturbation at the surface) and the extrema of the pressure perturbation and potential temperature perturbation agreed well with each other (Table 3). The numbers in Table 3 are comparable to those of GR08. In the numerical results from the different grid resolutions simulated by using 5th-order basis polynomials, the potential temperature profiles tend to have more variations than those using 8th-order basis polynomials (Fig. 9b and c). The results of the 8th-order polynomials tend to be closer to the converged solution. The above results suggest that the numerical solution can be converged more quickly by using a higher order of basis polynomial. Furthermore, the results in this paper show that adequate convergence can be reached at grid resolutions finer than 100 m.

In order to investigate the characteristics of the convergence more clearly, a self-convergence test was carried out. For this test, a reference solution is obtained by using spatial resolution $\Delta\bar{x} = 25$ m and $\Delta\bar{z} = 64$ m and time-step size $\Delta t = 0.1$ s. It is noted that the model solutions for the four spatial resolutions of 400, 200, 100, and 50 m, which are shown above, were obtained with the fixed time step $\Delta t = 0.3$ s. Because our model used GLL points and a pressure-based vertical coordinate, the all-model solutions were interpolated to the equidistant grid of $\Delta x = 400$ and $\Delta z = 50$ and then used to evaluate errors. Here, we evaluated the error by using the relative L2 error defined by

$$\|q_{simulation}\|_{L_2} = \sqrt{\frac{\int_{\Omega} (q_{ref} - q_{simulation})^2 d\Omega}{\int_{\Omega} q_{ref}^2 d\Omega}}, \quad (35)$$

where $q_{simulation}$ and q_{ref} represent the model solution and reference solution, respectively. The resulting L2 norm of the error in the potential temperature perturbation θ' is plotted in Fig. 10. It is noted that at the highest resolution of $\Delta\bar{x} = 50$ m, the experimental convergence rate reaches the convergence rate 2, which depends on the accuracy of the time-split RK3 integration scheme in relatively uniform spacing in the vertical direction. Note that it could be theoretically 1st-order accuracy with resolution if non-uniform vertical spacing is used, since the centered difference scheme in the vertical direction is implemented. Additionally, it is shown that the error of the solutions of the 8th-order basis function is slightly smaller than that of the 5th-order basis function.

4.4 Inertia–gravity wave test

This test examines the evolution of a potential temperature perturbation θ' in a constant mean flow with a stratified atmosphere. This initial potential temperature perturbation θ' radiates symmetrically to the left and right in a channel with periodic lateral boundary conditions. The inertia–gravity wave test introduced by Skamarock and Klemp (1994) (hereafter, SK94) serves as a tool to investigate the accuracy for NH dynamics. We also used this experiment to check the consistency of the results at various resolutions. The parameters for the test were the same as those of SK94. The initial state was a constant Brunt-Väisälä frequency of $N = 0.01/\text{s}$ with a surface potential temperature of $\theta_0 = 300$ K and a uniform zonal wind of $\bar{u} = 20$ m/s. In order to trigger the wave, the initial potential temperature perturbation θ' was overlaid the above initial state and is given as

$$\theta'(x, z) = \theta_c \frac{\sin\left(\frac{\pi z}{z_c}\right)}{1 + \left(\frac{x - x_c}{a_c}\right)^2}, \quad (36)$$

where $\theta_c = 0.01$ K, $z_c = 10$ km, $x_c = 100$ km, and $a_c = 5$ km. The domain was defined as $(x, z) \in [0, 300] \times [0, 10]$ km². We used periodic lateral boundary conditions and no-flux

boundary conditions for both the bottom and top boundaries. The simulation was performed for 3000 s with no viscosity.

Fig. 11 shows the solution θ' at the initial time and at time 3000 s with horizontal resolution $\Delta\bar{x} = 250\text{m}$ and vertical resolution $\Delta\bar{z} = 250\text{m}$. For comparison, the figure uses the same contouring interval as in SK94 and Giraldo and Restelli (2008). The results were produced with 8th-order polynomials per element. We conducted the 2D NH model with various basis polynomial orders at the same resolution, and the simulated results were found to be very comparable. SK94 provides an analytic solution for the case of the Boussinesq equations; however, it is only valid for the Boussinesq equations and we used the fully compressible equations in our model. Using the analytic solution for only qualitative comparisons, we found that the extrema of our results are comparable to the analytic values. Compared with the results of Giraldo and Restelli (2008), for which the fully compressible equations were also used, our results appear very similar.

Fig. 12 shows profiles along 5000 m for various horizontal resolutions. All models show consistently identical solutions with symmetric distribution about the midpoint ($x = 160\text{km}$), which is the location to which the initial perturbation moved by the horizontal flow of 20 m/s after 3000 s. Even in coarser-resolution experiments, it does not exhibit phase errors, although the maxima and minima near the midpoint ($x = 160\text{km}$) are slightly damped. Table 4 shows the extrema of vertical velocities and potential temperature perturbations for the results of various horizontal resolutions after 3000 s. All the experiments give almost the same values for potential temperature perturbation, which is in the range $\theta' \in [-1.52 \times 10^{-3}, 2.83 \times 10^{-3}]$. These values are comparable to those of other studies. For example, GR08 gave the ranges of $\theta' \in [-1.51 \times 10^{-3}, 2.78 \times 10^{-3}]$ from the model based on the spectral-element and discontinuous-Galerkin methods. Additionally, Li et al. (2013), using the high-order conservative finite volume model, showed $\theta' \in [-1.53 \times 10^{-3}, 2.80 \times 10^{-3}]$.

4.5 Rising thermal bubble test

We also conducted the rising thermal bubble test to verify the consistency of the scheme in the model to simulate thermodynamic motion (Wicker and Skamarock 1998). This test considers the time evolution of warm air in a constant potential temperature environment for an atmosphere at rest. The air that is warmer than ambient air rises due to buoyant forcing,

which then deforms due to the shearing motion caused by gradients of the velocity field and eventually shapes the thermal bubble into a mushroom cloud. Because the test case has no analytic solution, the simulation results were evaluated qualitatively.

The initial conditions we used follow those of GR08 in which the domain for the case is defined as $(x, z) \in [0, 1]^2 \text{ km}^2$. We used no-flux boundary conditions for all four boundaries. The domain was initialized for a neutral atmosphere at rest with $\theta_0 = 300\text{K}$ in hydrostatic balance. The potential temperature perturbation to drive the motion is given as

$$\theta' = \begin{cases} 0 & \text{for } r > r_c \\ \frac{\theta_c}{2} \left[1 + \cos\left(\frac{\pi r}{r_c}\right) \right] & \text{for } r \leq r_c \end{cases}, \quad (37)$$

where $\theta_c = 0.5 \text{ K}$, $r = \sqrt{(x - x_c)^2 + (z - z_c)^2}$ with $(x_c, z_c) = (500, 350) \text{ m}$, and $r_c = 250 \text{ m}$. The model was run for a time of 700 s. It should be noted that an explicit Laplacian (∇^2) diffusion on coordinate surfaces was used with a viscosity coefficient of $\nu = 1 \text{ m}^2\text{s}^{-1}$ for all simulations of this test. The numerical diffusion was applied for momentum and potential temperature along the horizontal and vertical directions to eliminate erroneous oscillations at the small scale. Although this amount of diffusion might seem excessive, it was chosen because it allows the model to remain stable even after the bubble reaches the top boundary.

Fig. 13 shows the potential temperature perturbation, horizontal wind field, and vertical wind field for the simulations of the two resolutions of 20-m and 5-m horizontal and vertical grid spacings ($\Delta\bar{x}$ and $\Delta\bar{z}$), respectively, employing 5th-order basis polynomials. In both simulations, the fine structures in the numerical solutions are well depicted with a symmetric distribution at the midpoint and sharp discontinuities of the fields along the boundary lines of the bubble. At lower resolution, however, degradations in the solution are visible in the potential temperature perturbation and vertical wind, as illustrated by fluctuations in the values as well as the concave lines at the top of the bubble. It is noted that although the numerical solution of the model using the spatially centered FDM of Wicker and Skamarock (1998) shows spurious oscillations in the potential temperature field, the present simulations of 2D NH using SEM horizontally and FDM vertically is devoid of these oscillations.

We also show the vertical profiles of potential perturbation at $x = 500$ m after 700 s for various resolutions in Fig. 14. Simulations were run with the resolutions of 5, 10, and 20 m, where the resolutions given are defined for both the horizontal and vertical directions. The results of the 10-m and 5-m resolutions are almost identical. The result of the lowest 20-m resolution, however, shows a somewhat unresolved solution, in which the maximum value is underestimated and the phase shift is depicted. Time series for maximum potential temperature perturbation and maximum vertical velocity are shown in Fig. 15. In all simulations, the maximum vertical velocity increases as the maximum theta perturbation decreases. This shows that the thermal energy of the theta perturbation leads to the acceleration of the vertical velocity. This result agrees well with the study of Ahmad and Lindeman (2007).

5 Summary and Conclusions

The non-hydrostatic compressible Euler equations for a dry atmosphere were solved in a simplified 2D slice (X-Z) framework by using spectral element method (SEM) for the horizontal discretization and finite difference method (FDM) for the vertical discretization. The form of the Euler equations used here is the same as those used in the weather research and forecasting (WRF) model. We employed a hybrid sigma-pressure vertical coordinate, which can be converted exactly into a sigma-pressure coordinate at the level of the actual coding implementation.

For the spatial discretization, the spatial operators were separated into their horizontal and vertical components. In the horizontal components, the operators were discretized using SEM, in which high-order representations are constructed through the GLL grid points by Lagrange interpolations in elements. Using GLL points for both interpolation and integration results in a diagonal mass matrix, which means that the inversion of the mass matrix is trivial. In the vertical components, the operators were discretized using the third-order upwind-biased finite difference scheme for the vertical fluxes and centered differences for the vertical derivatives. The time discretization relied on the time-split third-order Runge-Kutta technique.

We presented results from idealized standard benchmark tests for large-scale flows (e.g., mountain wave tests) and for non-hydrostatic-scale flows (e.g., inertia-gravity wave, rising thermal bubble, and density current). The numerical results showed that the present dynamical core is able to produce high-quality solutions comparable to other published solutions. These

1 tests effectively revealed that the combined spatial discretization method of the spectral
2 element and finite difference methods in the horizontal and vertical directions, respectively,
3 offers a viable method for the development of a NH dynamical core. Further research will be
4 conducted to couple the present core with the existing physics packages and extend the 2D
5 slice framework to develop a 3D dynamical core for the global atmosphere in which the
6 cubed-sphere grid is used for the spherical geometry. Further work will also be needed to
7 implement a horizontal diffusion operator in physical space, although horizontal diffusion on
8 the coordinate surface was used in this study.

10 **Acknowledgements**

11 This work was carried out through the R&D project on the development of global
12 numerical weather prediction systems of the Korea Institute of Atmospheric Prediction
13 Systems (KIAPS) funded by the Korea Meteorological Administration (KMA). The first
14 author thanks Dr. Joseph B. Klemp for sharing his idea for the hybrid sigma-pressure
15 coordinate and also thanks Francis X. Giraldo for his assistance and his MA4245 course at the
16 Naval Postgraduate School, which introduced us to the spectral element method. The second
17 author gratefully acknowledges the support of KIAPS, the Office of Naval Research through
18 program element PE-0602435N, and the National Science Foundation (Division of
19 Mathematical Sciences) through program element 121670. We also thank the reviewers for
20 their constructive suggestions.

References

- Ahmad, N. and J. Lindeman, 2007: Euler solutions using flux-based wave decomposition. *Int. J. Numer. Meth. Fluids*, 54, 47-72.
- Denis, J., J. Edwards, K. J. Evans, O. N. Guba, P. H. Lauritzen, A. A. Mirin, A. St-Cyr, M.A. Taylor, and P.H. Worly, 2011: CAM-SE: a scalable spectral element dynamical core for the community atmosphere model. *Int. J. High Perform, Comput. Appl.* doi: 10.1177/1094342011428142
- Durran, D. R. and J. B. Klemp, 1983: A compressible model for the simulation of moist mountain waves. *Mon. Wea. Rev.*, 111, 2341-2360.
- Giraldo, F. X., 2001: A spectral element shallow water model on spherical geodesic grids. *Int. J. Numer. Meth. Fluids*, 35, 869–901.
- Giraldo, F. X., and T. E. Rosmond, 2004: A Scalable Spectral Element Eulerian Atmospheric Model (SEE-AM) for NWP: Dynamical Core Tests. *Mon. Wea. Rev.*, 132, 133-153.
- Giraldo, F. X., 2005: Semi-implicit time-integrators for a scalable spectral element atmospheric model. *Quart. J. Roy. Meteor. Soc.*, 131, 2431–2454.
- Giraldo, F. X. and M. Restelli, 2008: A study of spectral element and discontinuous Galerkin methods for the Navier-Stokes equations in nonhydrostatic mesoscale atmospheric modeling: equation sets and test cases. *Journal of computational physics* 227, 3849-3877.

- 1 Giraldo, F. X., J. F. Kelly, and E. M. Constantinescu, 2013: Implicit-Explicit Formulations for
2 a 3D Nonhydrostatic Unified Model of the Atmosphere (NUMA). *SIAM J. Sci.*
3 *Comp.* 35 (5), B1162-B1194.
- 4
- 5 Hundsdorfer, W., B. Koren, M. van Loon, and K. G. Verwer, 1995: A positive finite-
6 difference advection scheme. *Journal of Computational Physics*, 117, 35-46.
- 7
- 8 Kelly, J. F. and F. X. Giraldo, 2012: Continuous and discontinuous Galerkin methods for a
9 scalable three-dimensional nonhydrostatic atmospheric model: Limited-area
10 mode. *Journal of Computational Physics*, 231, 7988–8008.
- 11
- 12 Klemp, J. B., W. C. Skamarock, and J. Dudhia, 2007: Conservative split-explicit time
13 integration methods for the compressible nonhydrostatic equations. *Mon. Wea.*
14 *Rev.*, 135, 2897-2913.
- 15
- 16 Lauritzen, P., C. Jablonowski, M. Taylor, and R. Nair, 2010: Rotated versions of the
17 Jablonowski steady-state and baroclinic wave test cases: A dynamical core
18 intercomparison. *J. Adv. Model. Earth Syst.*, 2, 15,
19 doi:10.3894/JAMES.2010.2.15.
- 20
- 21 Li, X., C. Chen, X. Shen, and F. Xiao, 2013: A multimoment constrained finite-volume model
22 for nonhydrostatic atmospheric dynamics. *Mon. Wea. Rev.*, 141, 1216-1240.
- 23
- 24 Park, S. -H., W. C. Skamarock, J. B. Klemp, L. D. Fowler, and M. G. Duda, 2013: Evaluation
25 of global atmospheric solvers using extensions of the Jablonowski and
26 Williamson baroclinic wave test case. *Mon. Wea. Rev.*, 141, 3116-3129.
- 27

- 1 Satho, M., T. Matsuno, H. Tomita, H. Miura, T. Nasuno, and S. Iga, 2008: Nonhydrostatic
2 icosahedral atmospheric model (NICAM) for global cloud resolving simulations.
3 Journal of Computational Physics, 227, 3486-3514.
- 4
- 5 Schär, C., D. Leuenberger, O. Fuhrer, D. Lüthi, and C. Girard, 2002: A new terrain-following
6 vertical coordinate formulation for atmospheric prediction models. Mon. Wea.
7 Rev., 130, 2459-2480.
- 8
- 9 Skamarock, W. C. and J. B. Klemp, 1994: Efficiency and accuracy of the Klemp-Wilhelmson
10 time-splitting technique. Mon. Wea. Rev., 122, 2623-2630.
- 11
- 12 Skamarock, W. C., J. B. Klemp, J. Dudhia, D. O. Gill, D. M. Barker, M. G. Duda, X. Y.
13 Huang, W. Wang, and J. G. Powers, 2008: A description of the advanced
14 research WRF version 3. NCAR Tech. Note TN-475+STR.
- 15
- 16 Skamarock, W. C. and J. B. Klemp, 2008: A time-split nonhydrostatic atmospheric model for
17 weather research and forecasting applications. Journal of Computational Physics,
18 227, 3465-3485.
- 19
- 20 Skamarock, W. C. J. B. Klemp, M. G. Duda, L. D. Fowler, and S. -H. Park, 2012: A
21 multiscale nonhydrostatic atmospheric model using centroidal Voronoi
22 tessellations and C-grid staggering. Mon. Wea. Rev., 140, 3090-3105.
- 23
- 24 Straka, J. M., R. B. Wilhelmson, L. J. Wicker, J. R. Anderson, and K. K. Droegemeier, 1993:
25 Numerical solutions of a non-linear density current: A benchmark solution and
26 comparisons. Int. J. Numer. Methods Fluids, 17, 1-22.
- 27
- 28 Taylor, M., J. Tribbia, and M. Iskandarani, 1997: The spectral element method for the shallow
29 water equations on the sphere. Journal of computational physics 130, 92-108.

- 1
- 2 Taylor, M., J. Edwards, S. Thomas, and R. Nair, 2007: A mass and energy conserving spectral
3 element atmospheric dynamical core on the cubed-sphere grid. J. Phys. Conf.
4 Ser., 78, 012074, doi:10.1088/1742-6596/78/1/012074
- 5
- 6 Thomas, S. J. and R. D. Loft, 2002: Semi-implicit spectral element atmospheric model.
7 Journal of Scientific Computing, 17, 339-350.
- 8
- 9 Thomas, S. J. and R. D. Loft, 2005: The NCAR spectral element climate dynamical core:
10 semi-implicit Eulerian formulation. Journal of scientific computing, 25, 307-322.
- 11
- 12 Wicker, L. J. and W. C. Skamarock, 1998: A time-splitting scheme for the elastic equations
13 incorporating second-order Runge-Kutta time differencing. Mon. Wea. Rev.,
14 126, 1992-1999.
- 15

1 Table 1. Summary of the resolutions and time-step sizes used for the tests.

Experiment	Resolution (m)	Time-step size (s)
Linear hydrostatic mountain wave	(5th-order basis function) $\Delta\bar{x} = 2000$ and $\Delta\bar{z} = 375$	$\Delta t = 20$
Simulations over the Schär Mountain	(5th-order basis function) $\Delta\bar{x} = 300$ and $\Delta\bar{z} = 250$	$\Delta t = 3$
2D density current	(5th- and 8th-order basis function) $\Delta\bar{x} = 400$ and $\Delta\bar{z} = 64$ $\Delta\bar{x} = 200$ and $\Delta\bar{z} = 64$ $\Delta\bar{x} = 100$ and $\Delta\bar{z} = 64$ $\Delta\bar{x} = 50$ and $\Delta\bar{z} = 64$	$\Delta t = 0.3$
Inertia-gravity wave	(8th-order basis function) $\Delta\bar{x} = 1250$ and $\Delta\bar{z} = 250$ $\Delta\bar{x} = 500$ and $\Delta\bar{z} = 250$ $\Delta\bar{x} = 250$ and $\Delta\bar{z} = 250$ $\Delta\bar{x} = 125$ and $\Delta\bar{z} = 250$	$\Delta t = 1$
Rising thermal bubble	(5th-order basis function) $\Delta\bar{x} = 20$ and $\Delta\bar{z} = 20$ $\Delta\bar{x} = 10$ and $\Delta\bar{z} = 10$ $\Delta\bar{x} = 5$ and $\Delta\bar{z} = 5$	$\Delta t = 0.2$ $\Delta t = 0.1$ $\Delta t = 0.05$

2

1 Table 2. Root-mean-square errors of the Schär Mountain wave after 10 h for $\Delta\bar{x} = 300$
2 m using 5th-order polynomials per element and $\Delta\bar{z} = 250$ m using 80 levels.

Variable	RMSE
u (m s ⁻¹)	1.43×10^{-1}
w (m s ⁻¹)	3.97×10^{-2}
θ (K)	3.77×10^{-2}

3

4

Table 3. Comparison between 5th- and 8th-order polynomials per element for the density current. The simulation was conducted with a resolution of $\Delta\bar{x} = 50$ m and $\Delta\bar{z} = 50$ m.

Order of polynomials	Front location (km)	ρ'_{\max} (Pa)	ρ'_{\min} (Pa)	θ'_{\max} (K)	θ'_{\min} (K)
5th	14.77	630.62	-452.79	0.08	-8.87
8th	14.74	626.91	-456.84	0.08	-8.94

Table 4. Comparison of the numerical results for various horizontal resolutions for the inertia–gravity wave. All simulations use 8th-order polynomials per element and a vertical resolution of $\Delta\bar{z} = 250$ m.

Resolution (m)	w_{\max} (m/s)	w_{\min} (m/s)	θ'_{\max} (K)	θ'_{\min} (K)
$\Delta\bar{x} = 125$	2.85×10^{-3}	-2.89×10^{-3}	2.83×10^{-3}	-1.52×10^{-3}
$\Delta\bar{x} = 250$	2.80×10^{-3}	-2.82×10^{-3}	2.83×10^{-3}	-1.52×10^{-3}
$\Delta\bar{x} = 500$	2.73×10^{-3}	-2.73×10^{-3}	2.83×10^{-3}	-1.52×10^{-3}
$\Delta\bar{x} = 750$	2.72×10^{-3}	-2.70×10^{-3}	2.83×10^{-3}	-1.52×10^{-3}
$\Delta\bar{x} = 1250$	2.68×10^{-3}	-2.62×10^{-3}	2.82×10^{-3}	-1.52×10^{-3}

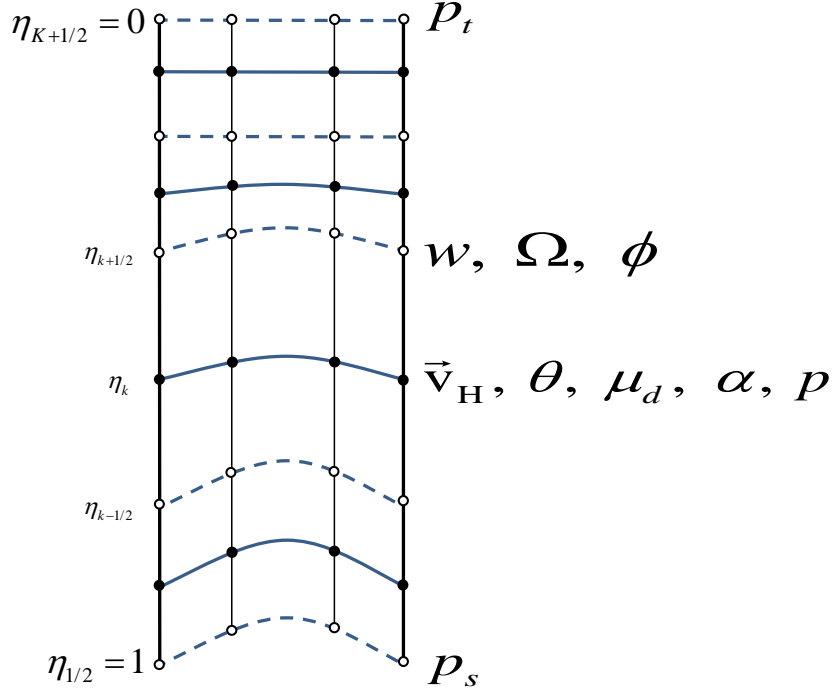


FIG. 1. Grid points of columns within an element having four GLL points. The hybrid-sigma coordinates are illustrated, and the closed (open) circles on the solid (dashed) line indicate the location of the variables at layer mid-points (interfaces).

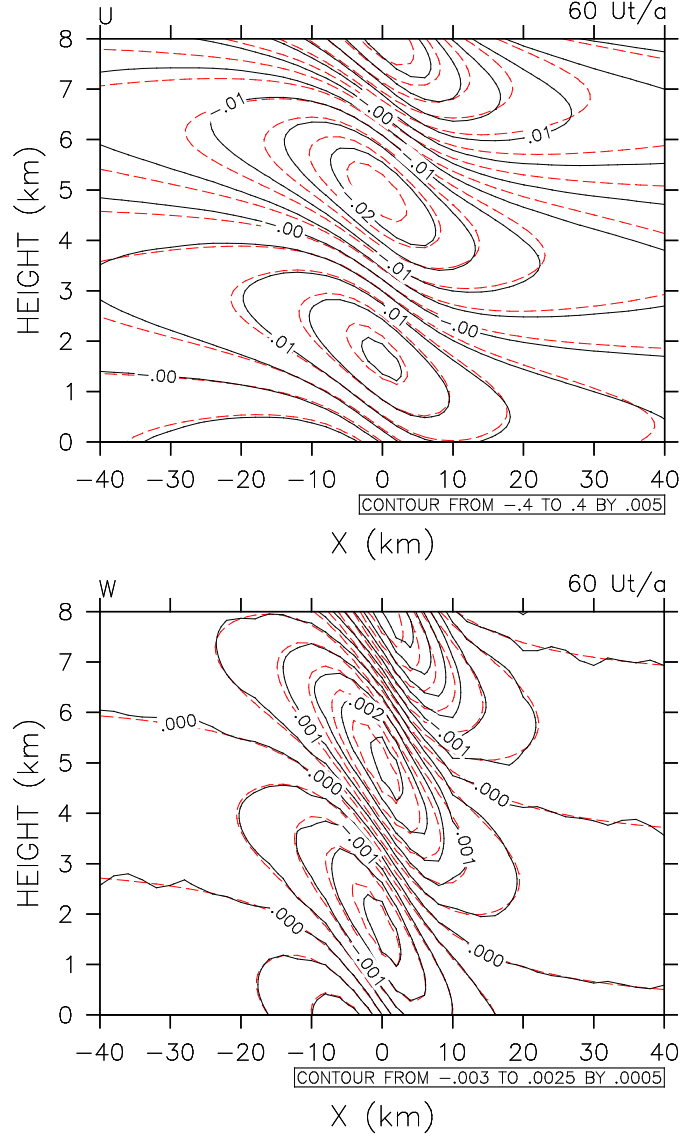


FIG. 2. Steady-state flow of (top) horizontal velocity (m/s) and (bottom) vertical velocity (m/s) over 1-m high mountain at nondimensional time $\frac{\bar{u}t}{a} = 60$ with a grid resolution of $\Delta\bar{x} = 2$ km using 5th-order basis polynomials per element and $\Delta\bar{z} = 375$ m. The numerical solution is represented by solid lines and the analytic solution is represented by dashed lines.

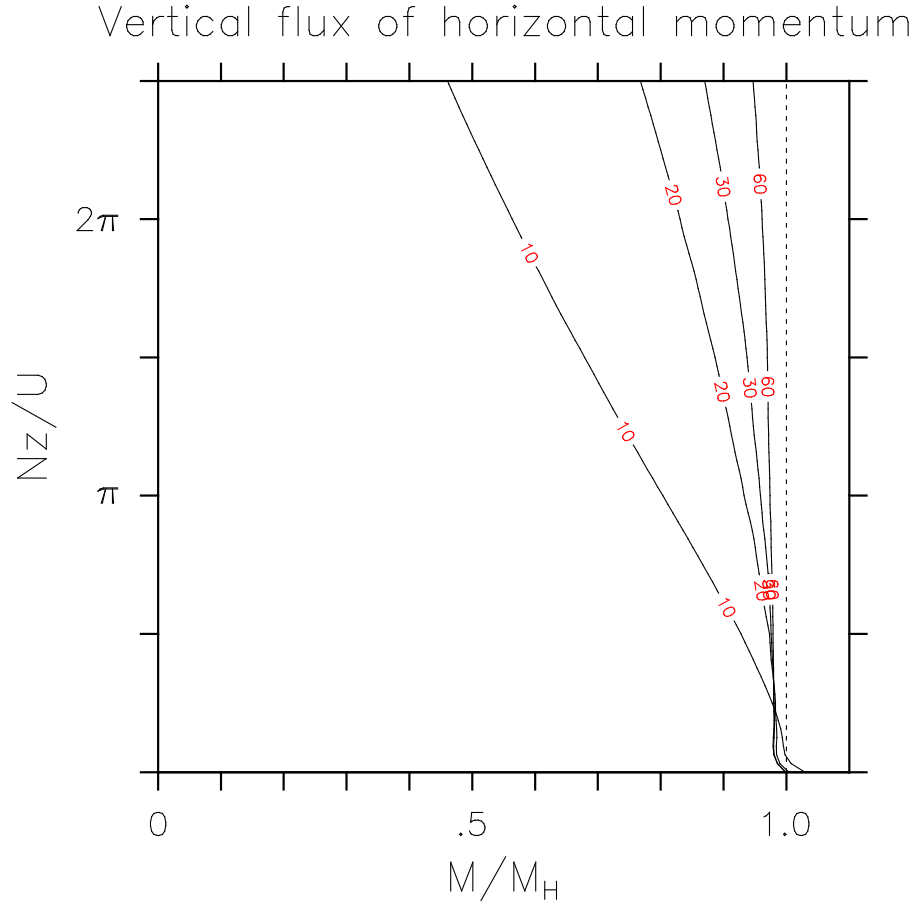


FIG. 3. Vertical flux of horizontal momentum, normalized by its analytic value at several nondimensional times $\frac{\bar{u}t}{a}$. M and M_H are the momentum flux of the numerical and analytic solutions.

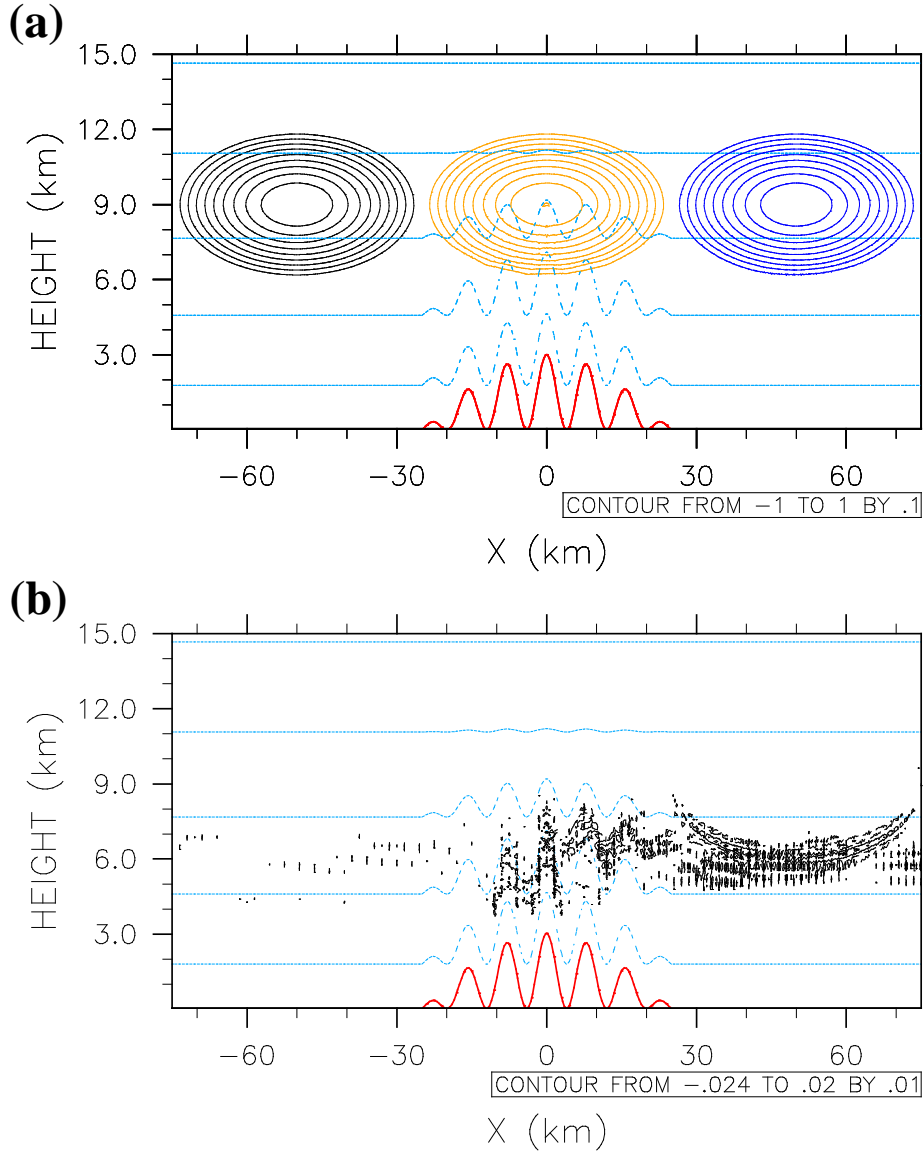


FIG. 4. Tracer advection test over the topography (red line). (a) Advective tracer at time 0 (black line), 2500 s (orange), and 5000 s (blue). The contour values are from -1.0 to 1.0 with an interval of 0.1 . (b) Error at time 5000 s. The contour values are from -0.24 to 0.2 with an interval of 0.01 . The numerical solutions were obtained with a grid resolution of $\Delta\bar{x} = 300$ m using 5th-order basis polynomials per element and $\Delta\bar{z} = 250$ m. The sky-blue dashed lines indicate surfaces of constant η . The zero contour level is omitted.

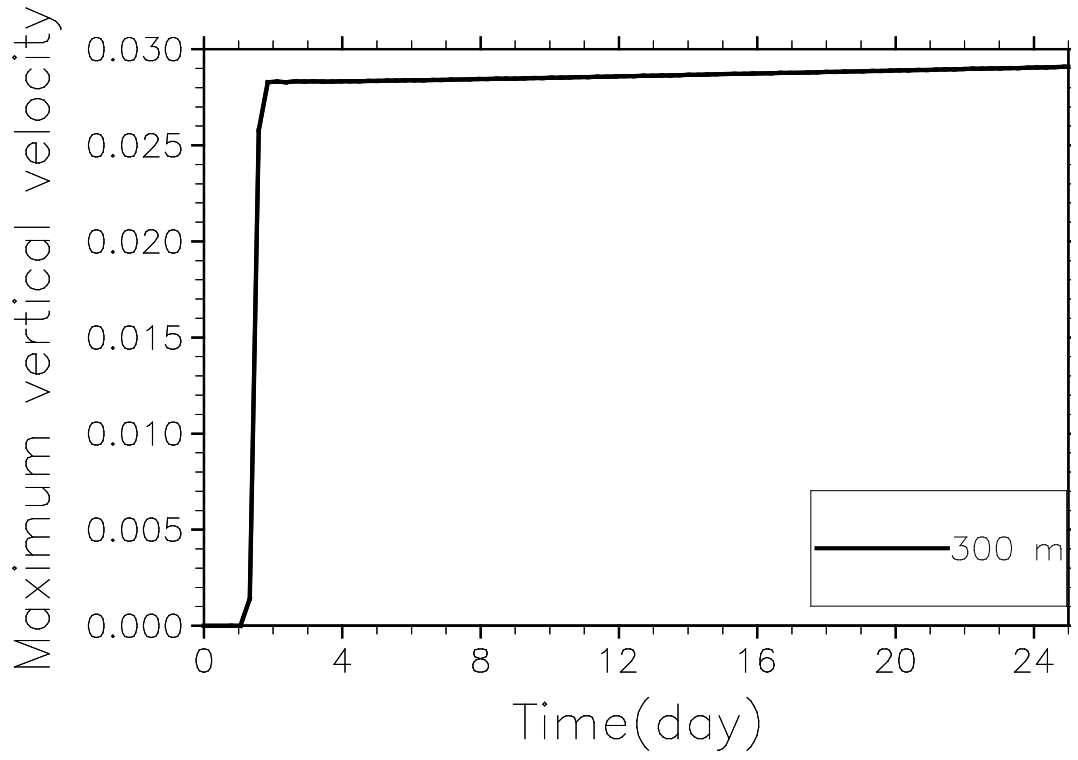


FIG. 5. Time series of the maximum vertical velocity for a resting-atmosphere simulations with a grid resolution of $\Delta\bar{x} = 300$ m using 5th-order basis polynomials per element and $\Delta\bar{z} = 250$ m.

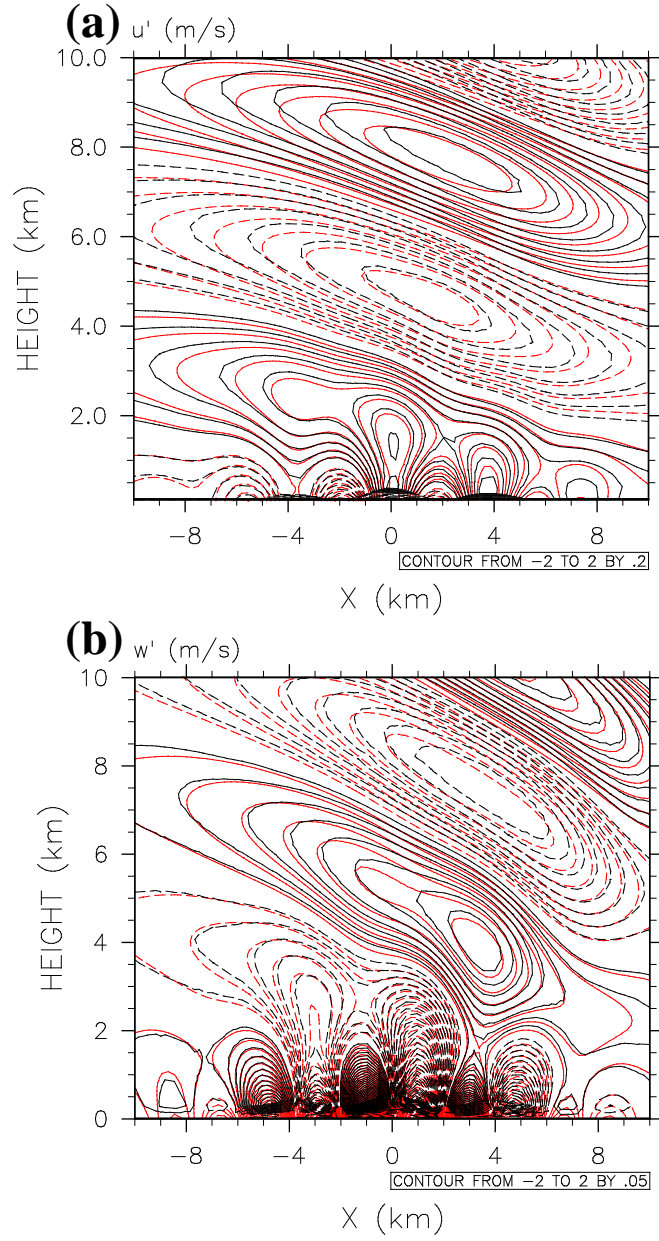


FIG. 6. Steady-state flow of (a) perturbed horizontal velocity (m s^{-1}) and (b) vertical velocity (m s^{-1}) over Schär Mountain after 10 h with a grid resolution of $\Delta\bar{x} = 300$ m using 5th-order basis polynomials per element and $\Delta\bar{z} = 250$ m. The numerical solution is represented by black lines and the analytic solution is represented by red lines. Dashed lines denote negative values. The contour values are from -2.0 to 2.0 with an interval of 0.2 (0.05) for the horizontal velocity (the vertical velocity).

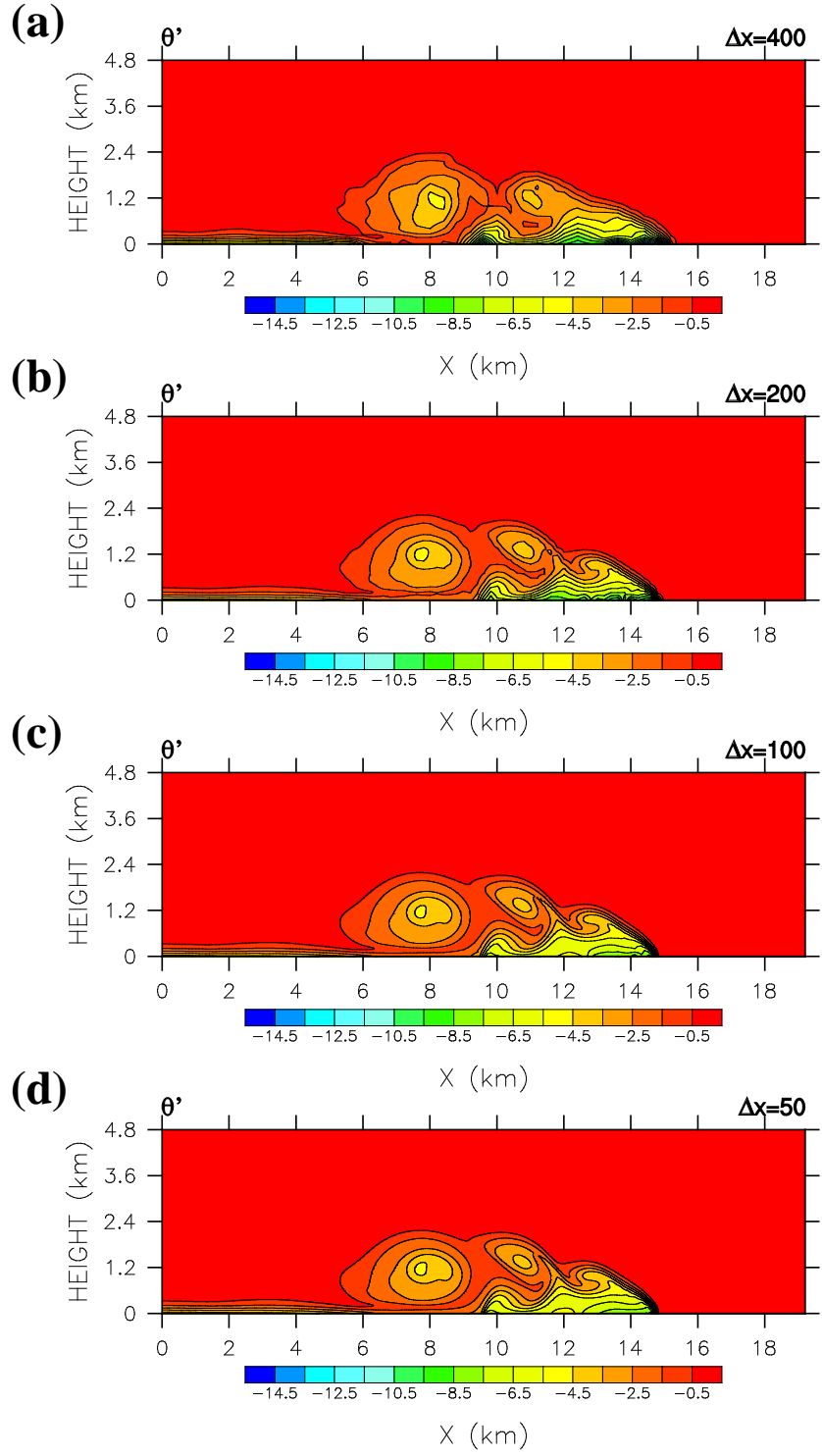


FIG. 7. Potential temperature perturbation after 900 s using grid spacing of (a) $\Delta \bar{x} = 400$ m, (b) $\Delta \bar{x} = 200$ m, (c) $\Delta \bar{x} = 100$ m, and (d) $\Delta \bar{x} = 50$ m, with 5th-order basis polynomials per element for the density current. All simulations use $\Delta \bar{z} = 64$ m grid spacing. The contour values are from -14.5 to -0.5 with an interval of 1.0 .

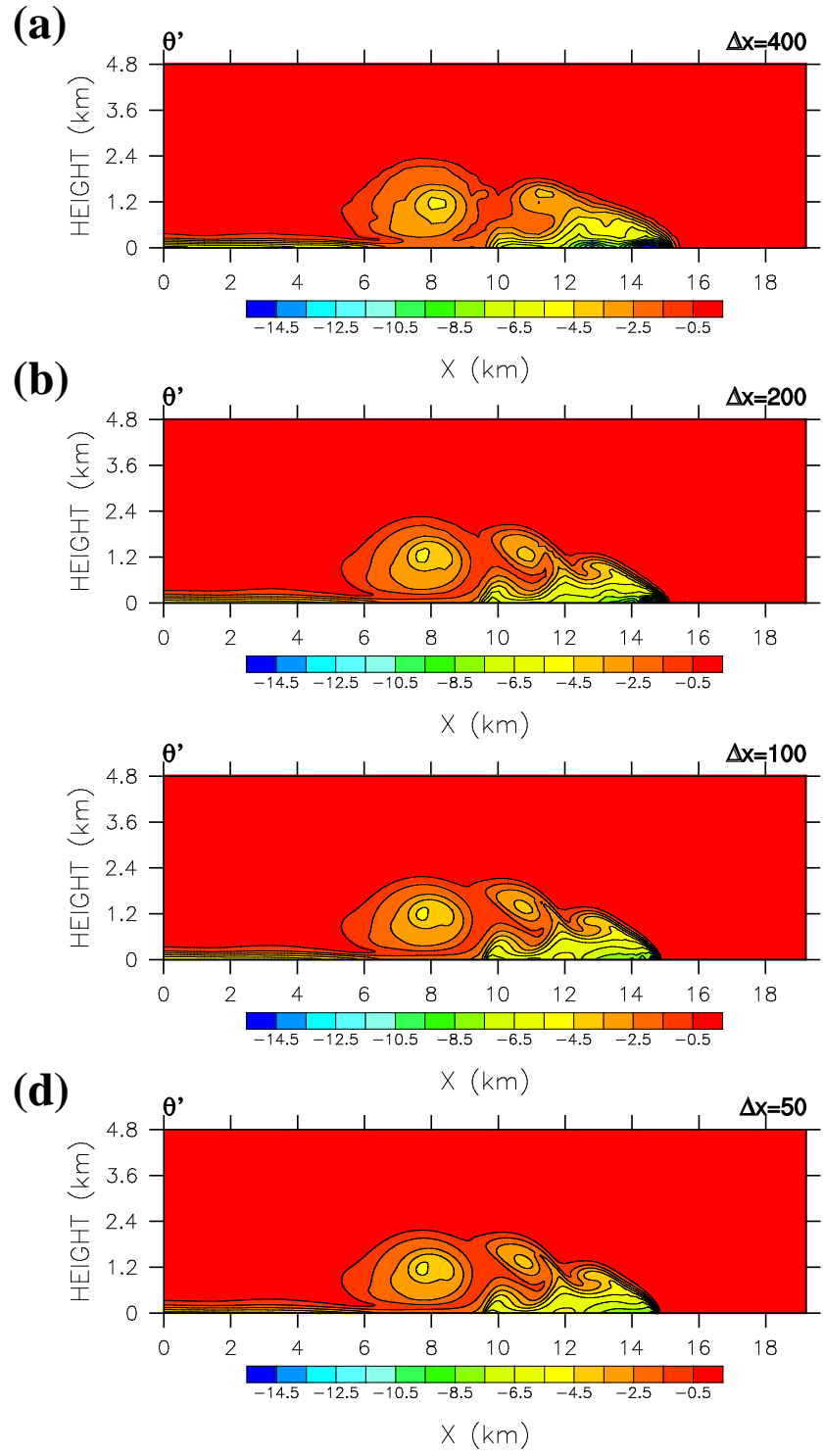


FIG. 8. As in Fig. 7, but with 8th-order basis polynomials per element.

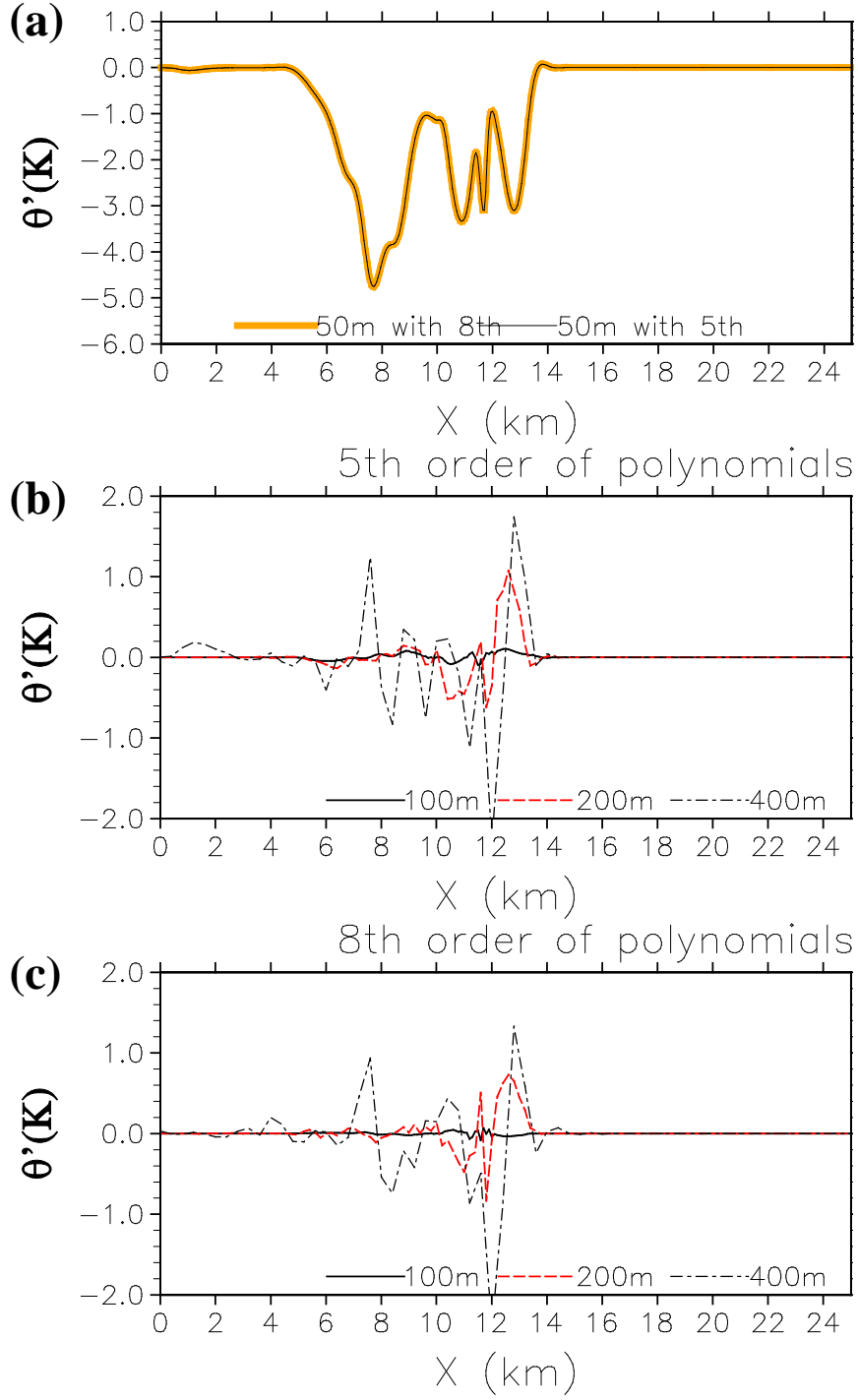


FIG. 9. Profiles of (a) potential temperature perturbation after 900 s along 1200 m height using grid spacing of $\Delta\bar{x} = 50$ m with 5th-order (thin solid line) and 8th-order (thick solid line) basis function, (b) difference between various resolution and $\Delta\bar{x} = 50$ m with 5th-order basis function, (c) difference between various resolution and $\Delta\bar{x} = 50$ m with 8th-order basis function.

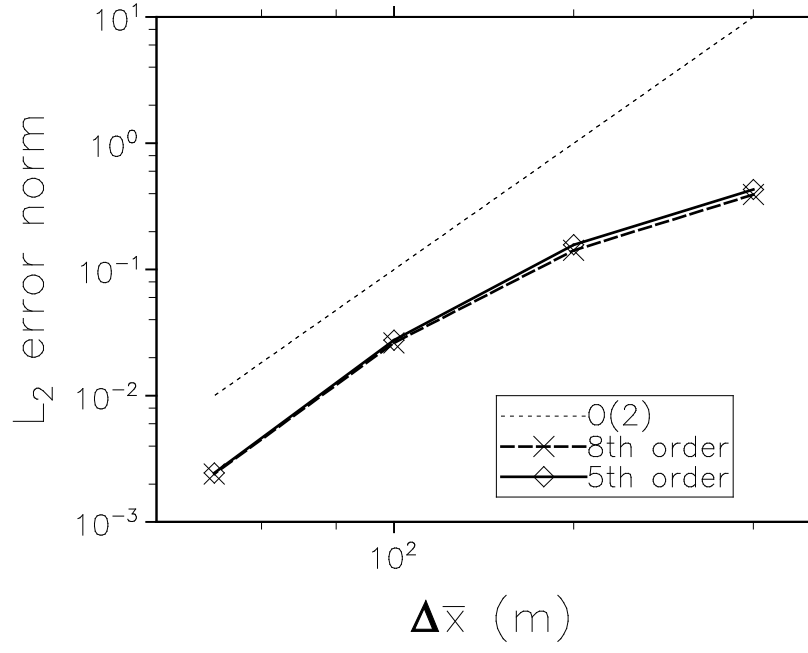


FIG. 10. Self-convergence test for the density current test; Relative L_2 error norms of the potential temperature perturbation θ' as functions of the space resolution $\Delta \bar{x}$ are shown. The reference solutions for these computations were made with $\Delta \bar{x} = 25$ m, $\Delta \bar{z} = 64$ m, and $\Delta t = 0.1$ s. The dotted line represents second-order convergence.

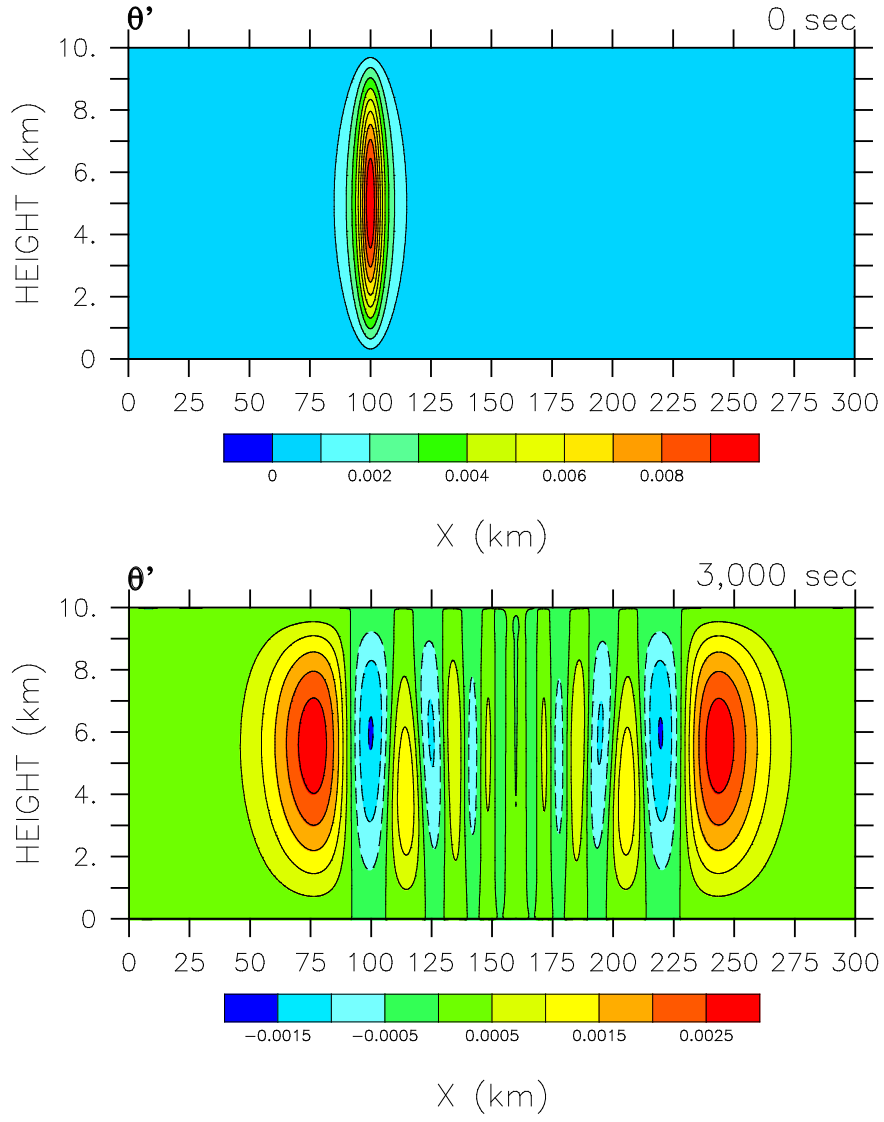


FIG. 11. Potential temperature perturbation at the initial time (top) and time 3000 s (bottom) for $\Delta\bar{x} = 250$ m using 8th-order basis polynomials per element and $\Delta\bar{z} = 250$ m for the inertia-gravity wave. The contour values are from 0 (−0.0015) to 0.009 (0.0025) with an interval of 0.001 (0.0005) for the initial time (time 3000 s).

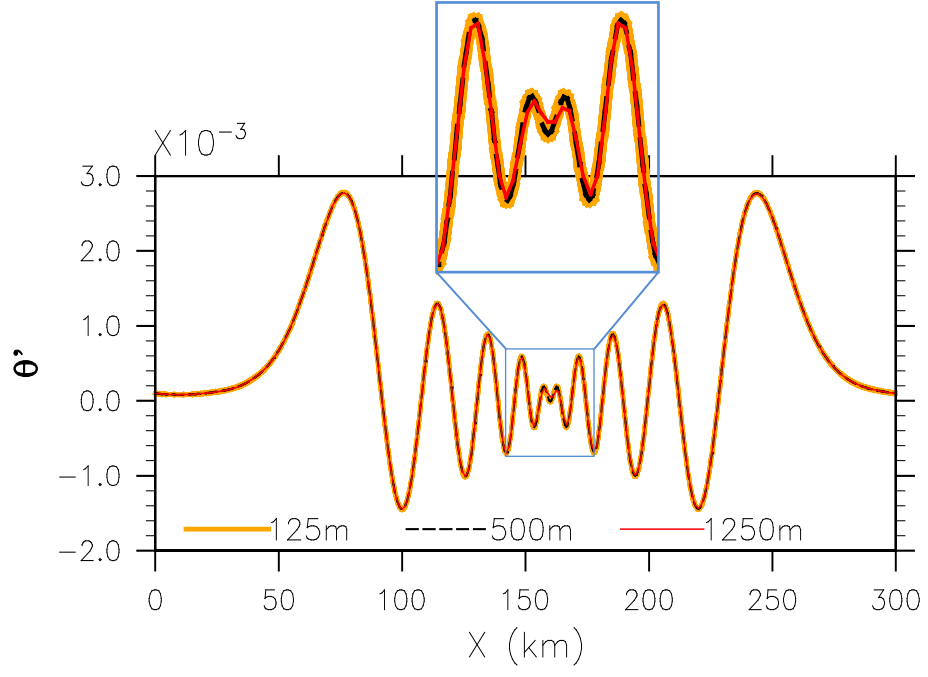


FIG. 12. Profiles of potential temperature perturbation along the 5000-m height for $\Delta\bar{x} = 125$ m (thick solid line), $\Delta\bar{x} = 500$ m (thin dashed line), and $\Delta\bar{x} = 1250$ m (thin solid line) using 8th-order basis polynomials per element for the inertia-gravity wave. All models use $\Delta\bar{z} = 250$ m.

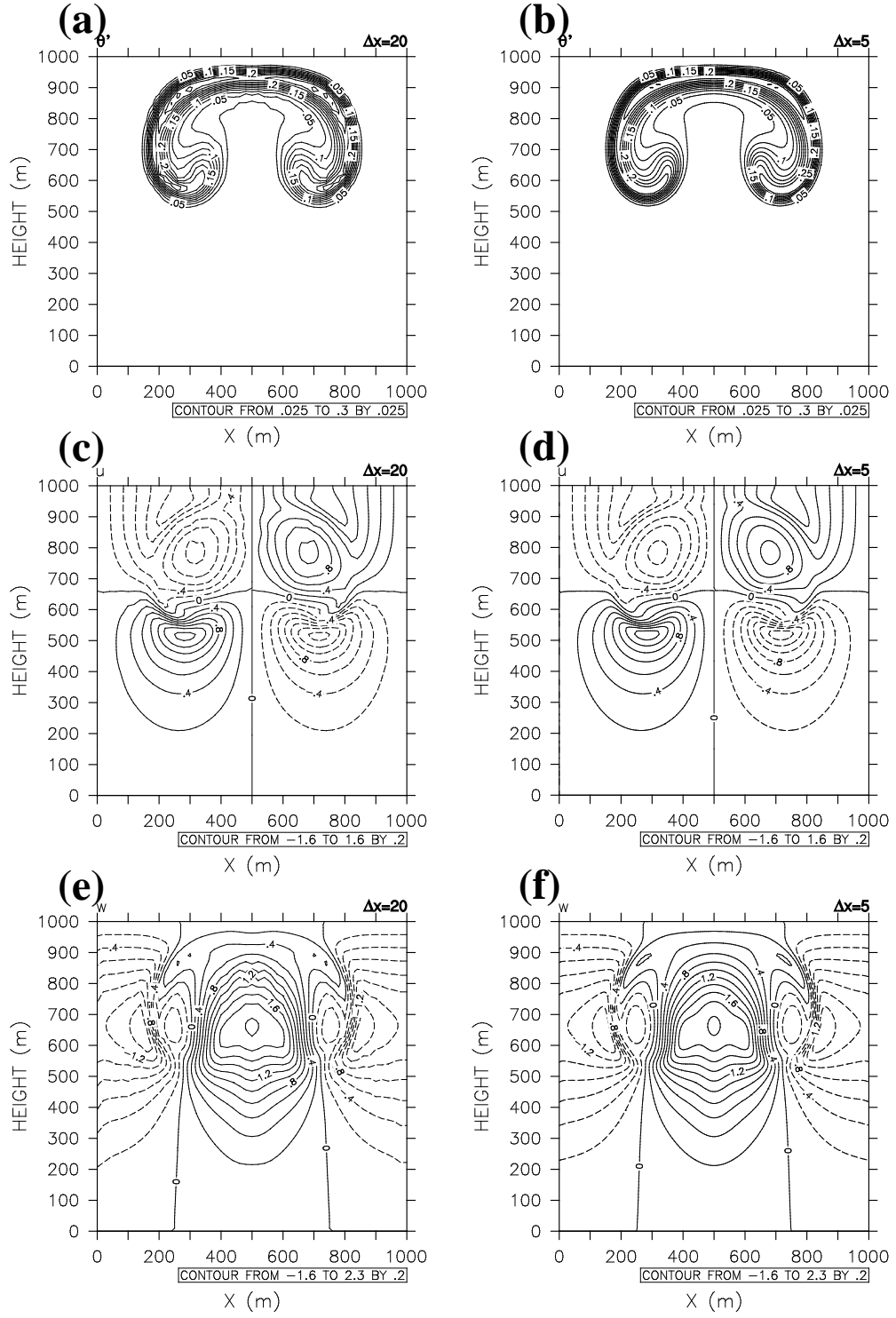


FIG. 13. Plots of (a, b) potential temperature perturbation (K), (c, d) horizontal wind (m/s), and (e, f) vertical wind (m/s) for the rising thermal bubble test after 700 s with (left) $\Delta\bar{x}, \Delta\bar{z} = 20$ m and (right) $\Delta\bar{x}, \Delta\bar{z} = 5$ m resolution for the rising thermal bubble test. All simulations use 5th-order basis polynomials per element. Negative values are denoted by dashed lines and positive values are denoted by solid lines.

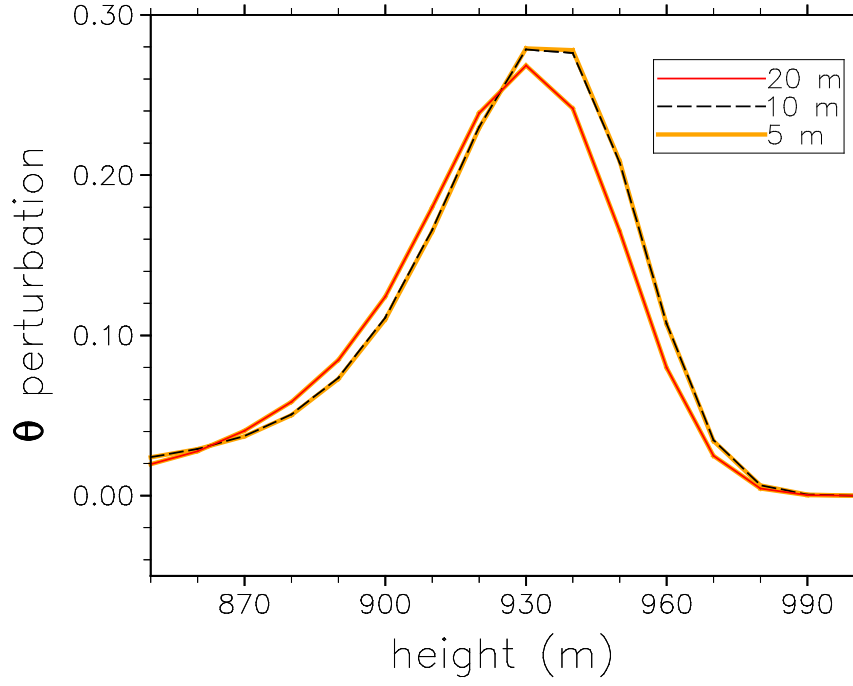


FIG. 14. Vertical profiles of the potential temperature perturbation for the rising thermal bubble test at $x = 500$ m after 700 s for various resolutions: $\Delta\bar{x}, \Delta\bar{z} = 20$ m (thin solid line), $\Delta\bar{x}, \Delta\bar{z} = 10$ m (thin dashed line), and $\Delta\bar{x}, \Delta\bar{z} = 5$ m (thick solid line).

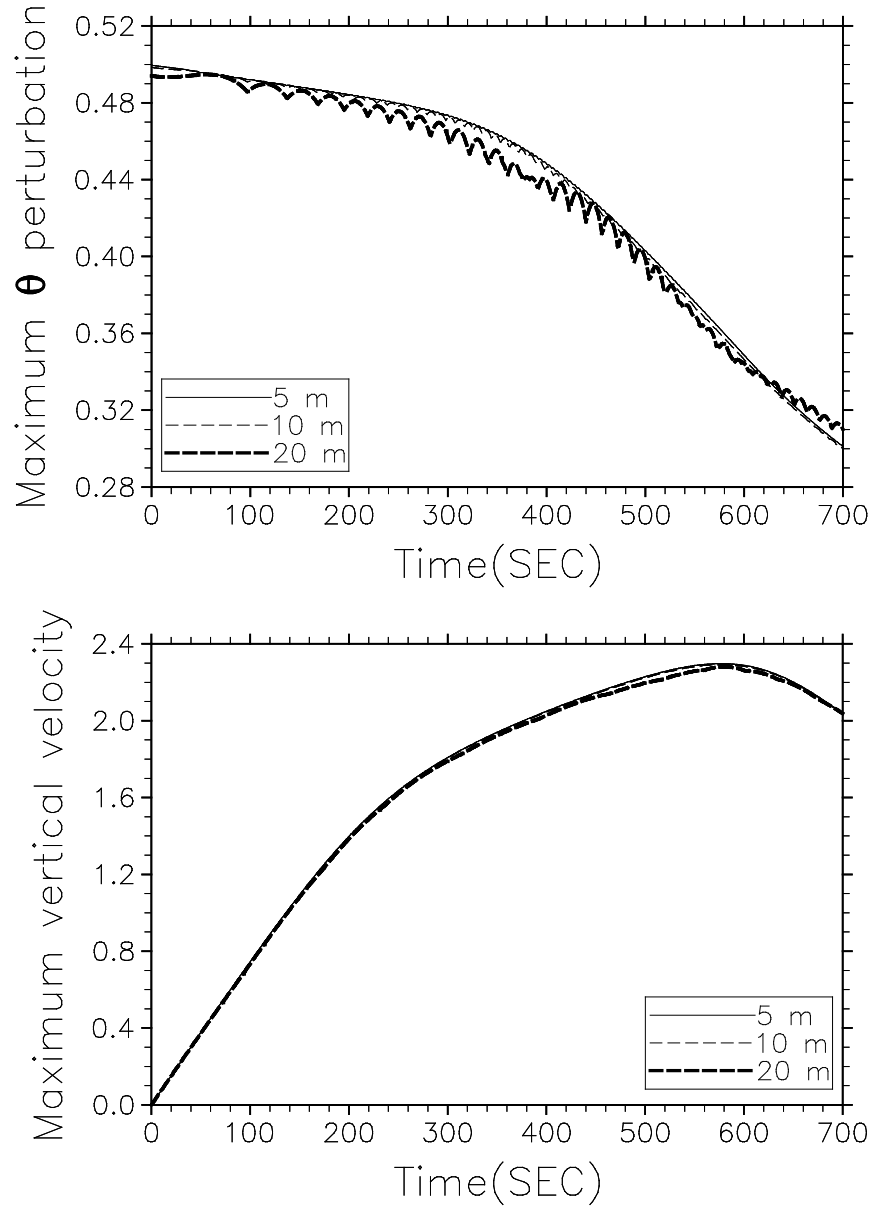


FIG. 15. Domain maximum potential temperature perturbation (top) and vertical wind (bottom) for the rising thermal bubble test. All simulations use 5th-order basis polynomials per element, and the vertical resolutions are the same as the horizontal resolutions.